Proceedings of the ASME 2020
Dynamic Systems and Control Conference
DSCC2020
October 4-7, 2020, Pittsburgh, PA, USA

DSCC2020-3238

A CONTROL-ORIENTED DYNAMICAL MODEL OF DEPOSITED DROPLET VOLUME IN ELECTROHYDRODYNAMIC JET PRINTING

Isaac A. Spiegel*
Department of Mechanical Engineering
University of Michigan
Ann Arbor, MI 48109
Email: ispiegel@umich.edu

Tom van de Laar
Department of Mechanical Engineering
Eindhoven University of Technology
5600 MB Eindhoven, The Netherlands
Email: t.j.v.d.laar@student.tue.nl

Tom Oomen
Department of Mechanical Engineering
Eindhoven University of Technology
5600 MB Eindhoven, The Netherlands
Email: t.a.e.oomen@tue.nl

Kira Barton
Department of Mechanical Engineering
University of Michigan
Ann Arbor, MI 48109
Email: bartonkl@umich.edu

ABSTRACT

Electrohydrodynamic jet printing (e-jet printing) is a nascent additive manufacturing process most notable for extremely high resolution printing and having a vast portfolio of printable materials. These capabilities make e-jet printing promising for applications such as custom electronics and biotechnology fabrication. However, reliably fulfilling e-jet printing's potential for high resolution requires delicate control of the volume deposited by each jet. Such control is made difficult by a lack of models that both capture the dynamics of volume deposition and are compatible with the control schemes relevant to e-jet printing. This work delivers such a model. Specifically, this work introduces a definition of "droplet volume" as a dynamically evolving variable rather than a static variable, and uses this definition along with analysis of high speed microscope videos to develop a hybrid dynamical system model of droplet volume evolution. This model is validated with experimental data, which involves the contribution of a novel technique for extracting consistent droplet volume measurements from videos.

*Address all correspondence to this author.

1 INTRODUCTION

Near-field electrohydrodynamic jet printing (e-jet printing) is an up-and-coming microscale resolution additive manufacturing (AM) technology in the family of liquid-form AM technologies such as inkjet printing. These technologies fabricate solid 2D patterns by ejecting fluid from a nozzle onto a substrate and solidifying that fluid by a process such as sintering or curing. More fluid can then be deposited atop the previously solidified fluid to build 3D structures in a layer-to-layer fashion [1].

E-jet printing's specific mechanism of fluid deposition revolves around the application of an electric field to the fluid meniscus at the tip of the nozzle. The field stresses the fluid surface in opposition to surface tension, elongating and sharpening the meniscus into a conical shape. Under weak fields, this "Taylor cone" may be stable. However, if the field is strong enough, a jet of fluid will issue from the cone tip, forming a contiguous bridge of fluid between the nozzle and substrate [2]. When this jet ultimately thins and pinches off or "breaks," a droplet of fluid is left on the substrate [3].

Figure 1 illustrates this concept for a standard e-jet printing configuration in which the electric field is generated by applying a voltage difference between the conductive fluid-filled nozzle

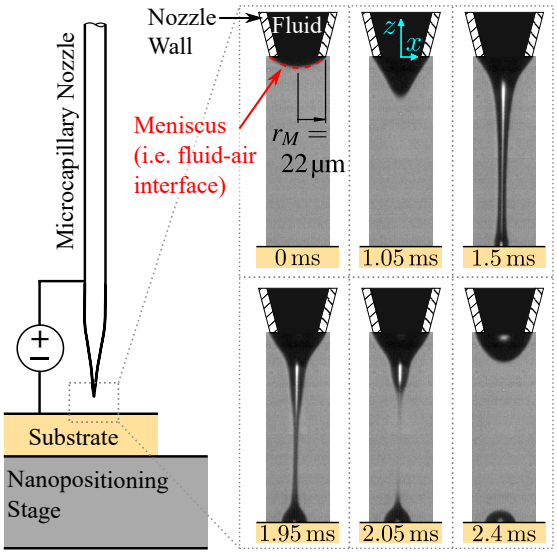

Figure 1. E-jet printing schematic and time lapse photography (with 0 ms at the rising edge of a voltage pulse) highlighting key stages of the ejection. The meniscus first elongates and sharpens before a jet forms between the nozzle and substrate. When flow from the nozzle ceases, the jet thins and breaks, depositing a droplet. The meniscus base radius r_M, determined by nozzle outer diameter, is 22 µm here, and in general can range from 1 µm to >100 µm. The coordinate system centered on the nozzle outlet is used to describe points on the fluid body.

and the substrate. A single ejection takes from 10 µs upwards to occur, depending on fluid properties. Time series state measurements are based on computer vision, as in [4].

E-jet printing stands apart from more established liquid-form AM technologies for two main reasons. First, it can print fluids with viscosities multiple orders of magnitude higher than inkjet printing's max viscosity [5]. Second, e-jet printing can achieve submicron line widths and gap sizes compared to inkjet printing's ∼10 µm minimum [3]. This is because the electrohydrodynamic jet thins considerably as it extends to strike the substrate while inkjet droplets pinch off the meniscus near the nozzle tip and thus have diameters approximately equal to that of the meniscus base. These advantages make e-jet printing attractive for fabricating printed and flexible sensors and other electronics [6–8], as well as for biotechnological applications [9, 10].

Reliably fulfilling the potential for submicron resolution requires closed-loop control for the rejection of disturbances introduced by variations in nozzle shape, fluid properties, and environmental factors like temperature and humidity [11]. However, the computer-vision-based measurement process is too slow compared to the jetting process for traditional real-time feedback control to be practical. Thus, recent research has focused on closing the loop in the iteration domain rather than the time domain. Specifically, this research uses measurements from previous trials of an e-jet printing task in conjunction with dynamical models of nominal system behavior to inform the feedforward control input signal for the subsequent trial [12–14], a technique known as iterative learning control (ILC).

Thus far, this research has been limited to using models of droplet spreading over a substrate to determine the droplet volume necessary for achieving a desired final print topography. It has not used knowledge of the dynamics between the applied voltage signal and the volume of fluid ultimately ejected from the nozzle, instead assuming perfectly known static relationships. Dynamical models outputting the volume deposited by each jet could be used to decouple the problems of learning the correct volume to deposit and learning the applied voltage signal necessary to achieve that volume, potentially decreasing the number of trials required to achieve satisfactory performance.

For a model to be compatible with ILC it must be founded on ordinary differential or difference equations. Of such control-oriented models developed for e-jet printing [15–17], only [17] models the material ejection process from beginning to end. This is done by modeling e-jet printing as a hybrid dynamical system: a collection of partial process models stitched together by a discrete event system in a mathematical structure closely related to piecewise system definition [18]. However, [17] does not explicitly model the deposited fluid volume, instead only modeling the volumetric flow rate of fluid out of the nozzle. This is in large part because past works have considered droplet volume ill-defined until the jet breaks, at which point the droplet volume was considered constant. Thus, there remains a gap between the prior art and satisfaction of the requirements that a model be both control-oriented and explicitly output deposited droplet volume.

The main contribution of the present work is a hybrid system model framework for e-jet printing that bridges this gap. Specifically, this work

(C1) defines the droplet volume as a dynamical state variable that may evolve over time,
(C2) presents a new division of the ejection process into partial processes to facilitate droplet volume modeling,
(C3) proposes and experimentally validates a mapping between nozzle flow rate and deposited droplet volume enabled by contributions (C1) and (C2), and
(C4) presents a new computer vision technique for taking consistent droplet volume measurements from high speed microscope video.

The remainder of the paper is organized as follows. Section 2 gives additional details of the e-jet printing process in order to clearly define the scope of this model's applicability. Section 3 presents the model (C1)-(C3). Section 4 presents the experimental methods for measurement, system identification, and model verification, including (C4). Section 5 presents and discusses the model verification results. Finally, concluding remarks are given in section 6.

2 E-JET PRINTING REGIME AND MODEL SCOPE

This work focuses on the subcritical drop on demand (DoD) jetting regime, first introduced in [4]. This regime is defined to capture the dynamics most useful for high resolution printing.

DoD or "pulsed" printing consists of applying a non-jetting low voltage, V_l, until a desired substrate-nozzle alignment is achieved. Then a pulse of high voltage V_h and duration T_p is fired, causing jetting. DoD printing, however, does not necessarily ensure that only one jet is fired per pulse. If T_p is long enough, multiple jets may occur sequentially under the system's autonomous electrohydrodynamics. Additionally, if V_h is too low, a jet may not fully form between the nozzle and substrate, and instead droplets may pinch off a partially elongated and/or blunted meniscus and fall, disconnected, to the substrate [19]. This repeated jetting and incomplete jetting represents both increased dynamical complexity if modeled in addition to complete single jetting, and potentially degraded performance due to enlarged droplet volumes.

Thus, this work requires V_h to be high enough to cause a contiguous jet, and requires subcritical pulse widths, meaning T_p must be small enough that the step down in applied voltage, rather than the autonomous system dynamics, causes the cessation of jetting. Because in this subcritical regime the nozzle flow rate is directly responsive to the control input, the dynamics in this printing regime can be reasonably modeled by linear time invariant (LTI) systems.

3 DYNAMICAL DEPOSITED VOLUME MODEL

3.1 Droplet Volume Definition

The plane of the nozzle outlet and the solid substrate surface provide obvious boundaries for a control volume (CV) through which the total volume of fluid outside the nozzle, $\mathcal{V}(t)$, and the total flow rate through the nozzle outlet, $Q(t)$, may be analyzed and modeled. Similarly, to analyze deposited droplet volume, $\mathcal{V}_d(t)$, as a dynamically evolving variable a droplet CV must be defined. This CV cannot be the same as the total fluid CV because only a fraction of the cumulative flow out of the nozzle up until the jet breaks is deposited on the substrate. The remainder of the fluid is retracted back into the nozzle under the power of surface tension after the jet breaks and the nozzle-connected fluid body and substrate-connected fluid body become disjoint.

This work introduces a CV with an upper boundary at the z-coordinate h_b, where the jet ultimately pinches closed and breaks into two disjoint fluid bodies, as shown in Figure 2. This CV allows measurements of droplet volume to be made as time series data while remaining consistent with prior notions of droplet volume in that after the jet breaks the volume of fluid in the droplet CV remains constant (assuming negligible evaporation).

To avoid dramatic increases in complexity, this work's model does not explicitly use h_b. The jet break point is only used to facilitate defining droplet volume as a time series signal

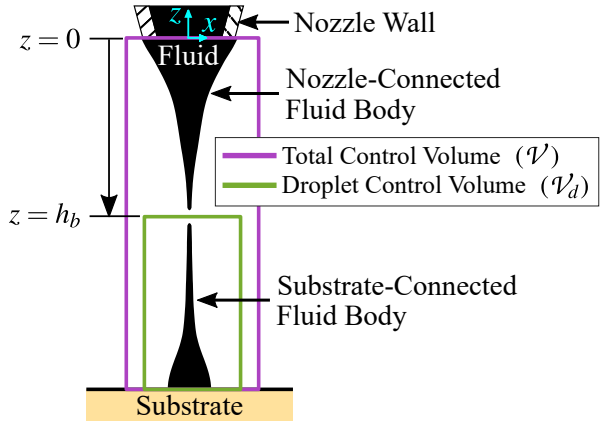

Figure 2. Schematic of the two CVs used in this work superimposed over an illustration of a jet immediately after breaking.

and for extracting time series measurements of droplet volume from microscope videos. Theoretical derivation of the jet break point's position is thus beyond the scope of this work, and it is estimated independently for each material ejection as described in Section 4.3.

3.2 Hybrid System Architecture

Ultimately, this work's model is given as the cascading of two discrete-time state-space systems with state transition formulas of the form $f : X \times U \times T \to X$ where X is the state vector space, U is the input vector space, and T is the time vector, all over the field $\mathbb{R}$. These two systems are the input-to-nozzle-flow-rate model

$$\begin{bmatrix} Q(t+T_s) \\ Q(t+2T_s) \end{bmatrix} = f_Q\left(\begin{bmatrix} Q(t) \\ Q(t+T_s) \end{bmatrix}, V(t)^2 - V_l^2, t\right), \quad (1)$$

and the nozzle-flow-rate-to-droplet-volume model

$$\begin{bmatrix} \mathcal{V}(t+T_s) \\ \mathcal{V}_d(t+Ts) \end{bmatrix} = f_{\mathcal{V}_d}\left(\begin{bmatrix} \mathcal{V}(t) \\ \mathcal{V}_d(t) \end{bmatrix}, \begin{bmatrix} Q(t) \\ Q(t+T_s) \end{bmatrix}, t\right). \quad (2)$$

T_s is the sample period in seconds, t is the time from the rising edge of the voltage pulse in seconds, and $V(t)$ is the applied voltage signal.

Both f_Q and $f_{\mathcal{V}_d}$ are piecewise defined to capture switching between partial process dynamics and to capture state resets—functions that execute upon certain switches and alter the dynamical states before the first evaluation of the newly active partial process dynamics.

In [17], the division of the material ejection process into partial processes was done to maximize the use of physics-driven

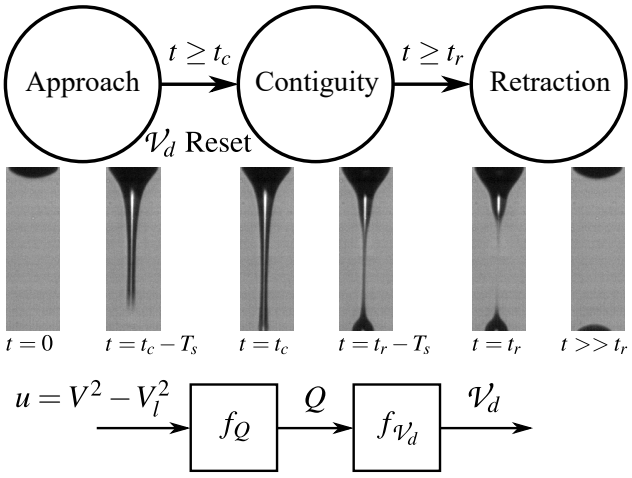

Figure 3. System Architecture. *Top:* Automaton illustrating the timed switching behavior of the system model and the reset determining the initial contiguity droplet volume. Each automaton location is accompanied by photographs of the first and final samples of the corresponding partial process from a video with $V_h = 1300\,\text{V}$ and $T_p = 1.5\,\text{ms}$. *Bottom:* Block diagram illustrating breakdown of a complete input-to-droplet-volume model into a nozzle flow rate model f_Q and a droplet volume model $f_{\mathcal{V}_d}$, both of which are piecewise defined to capture the switching and reset behavior of the automaton.

first principles model components, and was based on the stretching of the meniscus beyond its maximum stable non-jetting equilibrium extension.

This work presents an alternate breakdown of the material ejection process designed to facilitate modeling of the deposited droplet volume. This breakdown revolves around whether or not there exists a contiguous fluid stream between the nozzle and substrate, as the cessation of this contiguity is synonymous with the cessation of flow into or out of the droplet CV. Specifically, the complete process is broken into an "approach" stage, a "contiguity" stage, and a "retraction" stage. To better focus on the mapping between Q and $\mathcal{V}_d$, instead of modeling the meniscus tip position dynamics this work assumes that the timing of jet impingement and breaking are determined solely by the pulse parameters V_l, V_h, and T_p. Switching is thus governed by time: with the rising edge of the voltage pulse set to $t = 0$, transition from approach to contiguity occurs when t exceeds $t_c(V_l, V_h, T_p)$ and transition from contiguity to retraction occurs when t exceeds $t_r(V_l, V_h, T_p)$, where t_c and t_r are identified from data for each set of pulse parameters as described in Section 4.3.

The lone reset in the system is applied to $\mathcal{V}_d$ upon the switch from approach to contiguity. The complete model architecture is thus visualized by Figure 3.

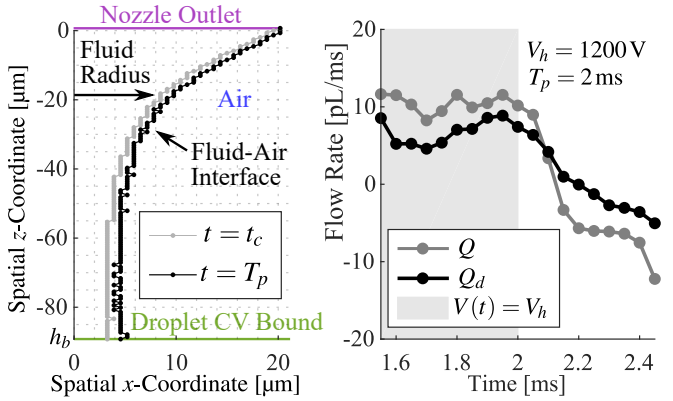

Figure 4. Measured data from a particular ejection video illustrating the motivation for a proportional Q_d model. *Left:* Half-outline of fluid body (the jet is roughly symmetric about z-axis) at the onset of contiguity and at the end of the voltage pulse, representing a 7% increase in volume outside the droplet CV. *Right:* Flow rate time series data during contiguity illustrating roughly proportional signals between Q and Q_d.

3.3 Deposited Droplet Volume Model

If the shape of the fluid-air interface were constant over time and the fluid incompressible, the volumetric flow rate out of the nozzle, Q, would be equal to the volumetric flow rate into the droplet control volume, Q_d. However, observation of video data indicates that the interface broadens slowly but steadily while voltage is high during contiguity. This implies that Q_d is only some fraction of Q. The video observation is corroborated by observation of the extracted time series data, such as that shown in Figure 4. This motivates a simple proportional model between Q and Q_d during contiguity:

$$Q_d(t) = b_{Q_d} Q(t) \tag{3}$$

where b_{Q_d} is a constant.

Trapezoidal integration of $Q_d(t)$ in equation (3) yields the first-order discrete-time droplet volume model for the contiguity stage

$$\mathcal{V}_d(t+T_s) = \mathcal{V}_d(t) + \frac{T_s}{2} b_{Q_d} Q(t+T_s) + \frac{T_s}{2} b_{Q_d} Q(t) \tag{4}$$

where $\mathcal{V}_d$ is the droplet volume and T_s is the sample period.

Volume is also added to the droplet CV during the approach stage when the tip of the meniscus crosses the upper boundary of the droplet CV but has not yet struck the substrate. However, each ejection video only provides a few samples of this situation, as the jet traverses the distance from the jet break position to the substrate relatively quickly. It may thus be impractical to identify a dynamical model of volume increase during the approach stage. Instead, this work sets $\mathcal{V}_d(t+T_s)$ to $\mathcal{V}_d(t)$ during

approach, and uses a reset to give $\mathcal{V}_d$ an initial condition in the contiguity stage, which accounts for the fluid added to the droplet CV during approach.

The total volume of the fluid outside the nozzle, $\mathcal{V}$, at the moment of jet collision with the substrate, t_c, may be roughly modeled as the volume of the Boolean union of a cylinder and a cone arranged to approximate the fluid body shape. $\mathcal{V}_d$ is then some fraction of the cylinder volume. This is equivalent to some fraction, ψ_0, of the total volume minus the Boolean difference of the cone and the cylinder, ψ_1. Physics-driven modeling of the jet diameter and break position necessary to explicitly calculate ψ_0 and ψ_1 are beyond the scope of this work, but the structure of the mapping between $\mathcal{V}$ and $\mathcal{V}_d$ at $t = t_c$ arising from this geometric analysis may still be used:

$$\mathcal{V}_d^+ = \mathcal{V}_d^- + \psi_0 \mathcal{V}^- + \psi_1 \tag{5}$$

where ψ_0 and ψ_1 require data-driven identification and the subscripts $+$ and $-$ indicate a state's value before and after reset. $\mathcal{V}_d^-$ will be 0 unless there was already fluid in the droplet control volume (e.g. if a second pulse is fired over an existing droplet).

Equation (5) requires total volume $\mathcal{V}$ be captured by the state dynamics, which can be done with a trapezoidal integration of the input Q similar to that of equation (3). This addition completes the hybrid model of droplet volume evolution in terms of total flow rate input, which can be given in totality as

$$\begin{bmatrix} \mathcal{V}(t+T_s) \\ \mathcal{V}_d(t+T_s) \end{bmatrix} = f_{\mathcal{V}_d}\left(\begin{bmatrix} \mathcal{V}(t+T_s) \\ \mathcal{V}_d(t+T_s) \end{bmatrix}, \begin{bmatrix} Q(t) \\ Q(t+T_s) \end{bmatrix}, t \right) = \begin{cases} \begin{bmatrix} \mathcal{V}(t) + \mathcal{Q} \\ \mathcal{V}_d(t) \end{bmatrix} & t < t_c \ \vee \ t \geq t_r \\ \begin{bmatrix} \mathcal{V}(t) + \mathcal{Q} \\ \psi_0 \mathcal{V}(t) + \mathcal{V}_d(t) + b_{Q_d} \mathcal{Q} + \psi_1 \end{bmatrix} & t_c \leq t < t_c + T_s \\ \begin{bmatrix} \mathcal{V}(t) + \mathcal{Q} \\ \mathcal{V}_d(t) + b_{Q_d} \mathcal{Q} \end{bmatrix} & t_c + T_s \leq t < t_r \end{cases} \tag{6}$$

where

$$\mathcal{Q} = \frac{T_s}{2} \left(Q(t+T_s) + Q(t) \right) \tag{7}$$

and $t < t_c$ corresponds to the approach stage, $t \geq t_r$ corresponds to the retraction stage, $t_c + T_s \leq t < t_r$ corresponds to all but the first time step of the contiguity stage, and $t_c \leq t < t_c + T_s$ corresponds to the first time step of contiguity, in which the reset is applied.

3.4 Nozzle Flow Rate Model

The main focus of this paper is the development and validation of the mapping between nozzle flow rate Q and deposited droplet volume $\mathcal{V}_d$. This could be done by simply injecting measured Q data into equation (6) and assessing the generated $\mathcal{V}_d$ signals against measured droplet volumes. However, for control there must ultimately be a model with input based on applied voltage $V(t)$ rather than $Q(t)$. To demonstrate the viability of equation (6) for this purpose, this section presents a simple V-to-Q model based on [17] which is cascaded with the $\mathcal{V}_d$ model.

The jetting model in [17] is a second-order LTI system, which may be represented in discrete time as

$$\begin{aligned} Q(t+2T_s) = a_{Q,1}(V_l, V_h, T_p) Q(t+T_s) + a_{Q,2}(V_l, V_h, T_p) Q(t) \\ + b_{Q,2}(V_l, V_h, T_p) u(t) \end{aligned} \tag{8}$$

where the input $u(t)$ is given as

$$u(t) = V(t)^2 - V_l^2 \tag{9}$$

This choice of input is made because the physics-based first principles models of flow rate are driven by the applied voltage squared, and because at the low voltage stable equilibrium, Q should be zero. The model parameters $a_{Q,1}$, $a_{Q,2}$, and $b_{Q,2}$ are identified independently for each pulse definition in [17].

[17] uses equation (8) when the nonlinear physics first principles models cease to capture the observed dynamics. This happens during contiguity and in approach and retraction when the meniscus is sufficiently elongated. Because the nonlinear models cannot capture the entirety of approach or contiguity, incorporating them into this work's deposited-volume-focused switching framework would substantially complicate the model. Thus to preserve the model's focus and manage complexity while still accounting for changes in dynamical behavior over the course of ejection, the structure of equation (8) is applied to the entire model with separate parameters identified for contiguity and non-contiguity partial processes. This results in the model

$$\begin{bmatrix} Q(t+T_s) \\ Q(t+2T_s) \end{bmatrix} = f_Q\left(\begin{bmatrix} Q(t) \\ Q(t+T_s) \end{bmatrix}, u(t), t \right) = \begin{cases} \begin{bmatrix} 0 & 1 \\ \tilde{a}_{Q,2} & \tilde{a}_{Q,1} \end{bmatrix} \begin{bmatrix} Q(t) \\ Q(t+T_s) \end{bmatrix} + \begin{bmatrix} 0 \\ \tilde{b}_{Q,2} \end{bmatrix} u(t) & t < t_c \ \vee \ t \geq t_r \\ \begin{bmatrix} 0 & 1 \\ \bar{a}_{Q,2} & \bar{a}_{Q,1} \end{bmatrix} \begin{bmatrix} Q(t) \\ Q(t+T_s) \end{bmatrix} + \begin{bmatrix} 0 \\ \bar{b}_{Q,2} \end{bmatrix} u(t) & t_c \leq t < t_r \end{cases}, \tag{10}$$

where the tilde-topped and overlined parameters are separately identified (and have the input arguments (V_l, V_h, T_p) dropped for compactness) and correspond to the approach and retraction stages and the contiguity stage, respectively.

Table 1. Experimental High Voltage and Pulse Width Pairs

V_h [V]	T_p [ms]	V_h [V]	T_p [ms]	V_h [V]	T_p [ms]
1100	2.0	1300	1.5	1350	2.0
1150	2.0	1300	1.8	1370	2.0
1200	2.0	1300	2.0	1420	1.5
1250	2.0	1300	2.3	1470	1.5

4 EXPERIMENTAL METHODS

4.1 Experimental Setup

The experimental setup in this work is identical to that of [4], which contains a thorough explanation and graphical depiction of the setup. In summary, a silicon wafer substrate is mounted on a nanopositioning stage (Aerotech, Planar$_{\text{DL}}$), a conductively coated microcapillary nozzle (World Precision Instruments TIP30TW1, 30 µm outlet inner diameter, 43.6 µm outlet outer diameter) is suspended with its tip 150 µm above the substrate, and a high speed camera (Vision Research, Phantom V9.0) operating at 20,000 frames per second ($T_s = 50\,\mu$s) with a 20x microscope lens assembly (yielding a 0.65 $\frac{\mu\text{m}}{\text{pixel}}$ resolution) is mounted with its optical axis parallel to the substrate and between the substrate and nozzle outlet. The nozzle and substrate are connected to the output and ground electrodes of a high voltage amplifier (TREK 677B) The fluid used is Norland Optical Adhesive 81 (dynamic viscosity 0.3 Pa s).

Twelve sets of (V_l, V_h, T_p) parameters, referred to as "experiments," are tested, with 20 trials of each experiment being recorded. All trials begin from the low voltage equilibrium meniscus position over a clean region of substrate with no prior fluid depositions: $V(0) = V_l$, $Q(0) = Q(T_s) = 0$, $\mathcal{V}_d(0) = 0$, and $\mathcal{V}(0)$ is the small total fluid volume outside the nozzle at low voltage equilibrium (see Figure 1, 0 ms). Time $t = 0$ is defined at the rising edge of the voltage pulse. $V_l = 525$ V for all experiments. V_h and T_p values are tabulated in Table 1.

4.2 High Speed Microscopy & State Extraction

Each frame of video is a grayscale image containing the nozzle tip, the fluid outside the nozzle, and—if there is fluid near enough to the substrate—a reflection of the fluid off of the substrate. The image processing protocol used to extract time series measurements of $\mathcal{V}$ and $\mathcal{V}_d$ from these images is nearly the same as that of [4]. Edge finding identifies the (x,z) coordinates for the silhouette of the nozzle tip, fluid, and reflection. Corner finding and extremum finding identify the z-coordinates of the nozzle-fluid interface and the substrate-fluid interface. Finally, the width of the silhouette at each z-coordinate is treated as the diameter of a disk of height equal to the image resolution (i.e. the height of one pixel) for volume determination. Q and Q_d measurements are numerical derivatives of $\mathcal{V}$ and $\mathcal{V}_d$ measurements. On top of this established procedure, this work introduces a method to harness the reflection for improving volume measurement consistency near the substrate and a method for estimating jet break position, both of which are illustrated in Figure 5 and explained in detail below.

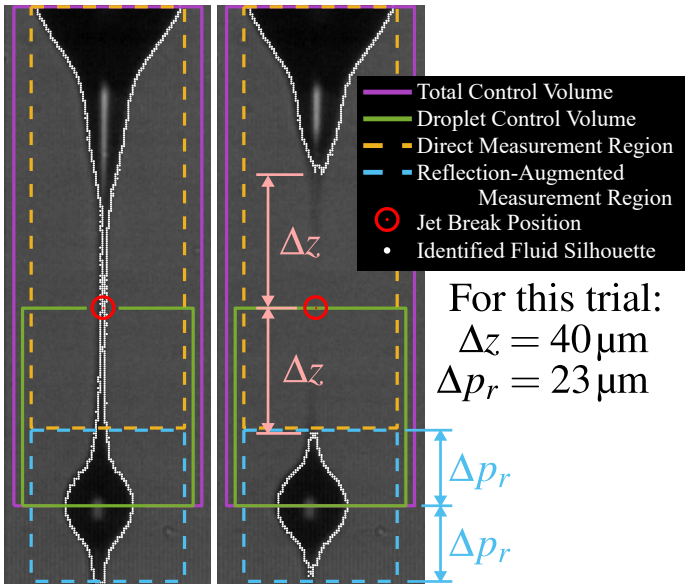

Figure 5. Depiction of the two CVs described in Section 3.1, the distinction between the direct and reflection-augmented measurement regions, and the estimated jet break position superposed on the final contiguity frame and first retraction frame for a particular trial ($V_h = 1300$ V, $T_p = 1.5$ ms). Δz is the distance from either fluid body tip to the jet break position.

In previous works, the reflection was eliminated from volume calculations entirely. However, due to the quantization error associated with fixing the substrate position measurement to a pixel edge (and possibly other optical or image processing imperfections), this direct calculation leads to nonzero flow of fluid through the bottom of the droplet CV as the droplet spreads. This change in droplet volume measurement during the retraction stage makes identifying a final droplet volume value difficult. Thus this work introduces reflection-augmented volume measurement to maintain conservation of volume near the substrate. Given images that extend Δp_r pixels below the estimated substrate position, a region $2\Delta p_r$ pixels tall centered on the estimated substrate position is defined as the "reflection-augmented measurement region." The volume of fluid contained in the upper half of this region (i.e. the portion of the region containing direct fluid silhouette rather than reflection) is taken as half the volume computed in the total reflection-augmented measurement region. In other words, the true fluid volume is taken as the average of the silhouette volume and reflection volume.

The jet break position for each trial is measured from the first video frame in which there are two disjoint fluid bodies (i.e. the first frame of retraction). The jet break position is estimated

to be the midpoint between the tips of these bodies based on the assumption that the initial droplet and meniscus tip velocities and accelerations are equal and opposite at the moment the jet breaks. This assumption is driven by the fact that the initial jet-breaking and retraction behavior is dominated by surface tension. While this assumption neglects much of the complexity of the true retraction physics, Figure 5 suggests it does an acceptable job of identifying the thinnest portion of the jet immediately before breaking, and it circumvents image resolution and noise issues associated with directly computing the thinnest jet point in the final frame of contiguity.

4.3 System Identification

The parameters to be identified can be grouped into two categories. First are the primary model parameters making up the dynamics of the Q-to-$\mathcal{V}_d$ model (6): b_{Q_d}, ψ_0, and ψ_1, which are constant over all experiments. Second are the supporting model parameters determining the timing of switching in the volume model (6) and the simulated nozzle flow rate model (10): $t_c(V_l,V_h,T_p)$, $t_r(V_l,V_h,T_p)$, $\tilde{a}_{Q,1}(V_l,V_h,T_p)$, $\tilde{a}_{Q,2}(V_l,V_h,T_p)$, $\tilde{b}_{Q,2}(V_l,V_h,T_p)$, $\overline{a}_{Q,1}(V_l,V_h,T_p)$, $\overline{a}_{Q,2}(V_l,V_h,T_p)$, and $\overline{b}_{Q,2}(V_l,V_h,T_p)$, whose values vary with the the experiment parameters. The measured data is divided evenly into training and validation data. For each experiment, 10 trials are reserved for training and 10 for validation.

In order to keep the timing of switching fixed to a particular sample, for each experiment t_c and t_r are taken as the median time of the first frame of contiguity and retraction over the 10 training trials of that experiment (1 parameter from 10 samples). All other parameters are identified via least squares regression. The model coefficients for equation (10) are trained independently for each experiment on all the available data in the corresponding process stage (3 parameters from 353 samples for approach and 194 samples for contiguity, on average). The reset parameters ψ_0 and ψ_1 are trained on the set of first frames of contiguity (i.e. the $t_c \leq t < t_c + T_s$ sample) from all trials (2 parameters from 120 samples). Finally, b_{Q_d} is trained on all contiguity training data (1 parameter from 2337 samples).

4.4 Error Metrics

This section presents metrics for validating the reflection-augmented volume measurement technique, and the ability of the total model to predict deposited droplet volume.

The improvement yielded by reflection-augmented volume measurement over direct measurement is quantified as the mean percent decrease in total variation of the filtered retraction-stage $\mathcal{V}_d$ timeseries between the two techniques. The total variation L of a time-varying parameter is its total change (as opposed to net change) over a given period of time T_L. In theory, the total variation of $\mathcal{V}_d$ in the retraction stage is zero, making its reduction a practical improvement metric. However, high frequency measurement noise also contributes to L. To moderate noise's influence, the $\mathcal{V}_d$ signal is filtered before its total variation is computed. Thus, the total variation of a trial j is given by

$$L_j = \sum_{t=t_r}^{t_r+T_L} |\mathcal{V}_d^f(t+T_s) - \mathcal{V}_d^f(t)| \tag{11}$$

where $\mathcal{V}_d^f$ is the filtered volume signal. The final metric for reflection-augmented volume measurement performance is

$$\Delta L\% = 100 \underset{j\in\text{All Validation Trials}}{\text{mean}} \frac{L_j^{\text{direct}} - L_j^{\text{augmented}}}{L_j^{\text{direct}}} \tag{12}$$

.

Here, a Savitzky-Golay filter with a window size of 15 samples is used. $T_L = 10\,\text{ms}$ (200 samples), roughly the time it takes for the droplet to spread and settle to its final shape on the substrate.

The efficacy of the overall model in predicting deposited droplet volume is measured by the mean unsigned error between the modeled $\mathcal{V}_d(t_r)$ (equal to $\mathcal{V}_d(t > t_r)$) and the measured final droplet volume. Measured final droplet volume is taken as

$$\mathcal{V}_{d,j}^{\text{final}} = \underset{t\in[t_r,t_r+10\,\text{ms}]}{\text{mean}} \mathcal{V}_{d,j}^{\text{meas}}(t) \tag{13}$$

where $\mathcal{V}_{d,j}^{\text{meas}}(t)$ is the measured droplet volume time series for a particular trial j, making the mean unsigned error

$$e_{\mathcal{V}_d} = \underset{j\in J}{\text{mean}} |\mathcal{V}_{d,j}^{\text{final}} - \mathcal{V}_{d,j}(t_r)| \tag{14}$$

This metric is evaluated over multiple sets of trials J. In addition to an aggregate $e_{\mathcal{V}_d}$ in which J contains the validation trials of all but one experiment (that of lowest V_h, see Section 5.2 for discussion of this exclusion), individual $e_{\mathcal{V}_d}$ values are computed for each experiment. This is done to examine how model performance changes with the pulse parameters. Additionally, for each of these sets J, both an $e_{\mathcal{V}_d}$ using $\mathcal{V}_d(t_r)$ generated from injecting measured nozzle flow rate into equation (6) and an $e_{\mathcal{V}_d}$ using $\mathcal{V}_d(t_r)$ generated from nozzle flow rate simulated by equation (10) are computed. This is done to enable both focus on the quality of equation (6) and broader consideration of the ultimate needs for a control-oriented e-jet printing model, respectively. Finally, along with each $e_{\mathcal{V}_d}$, a corresponding standard deviation of the signed error is presented.

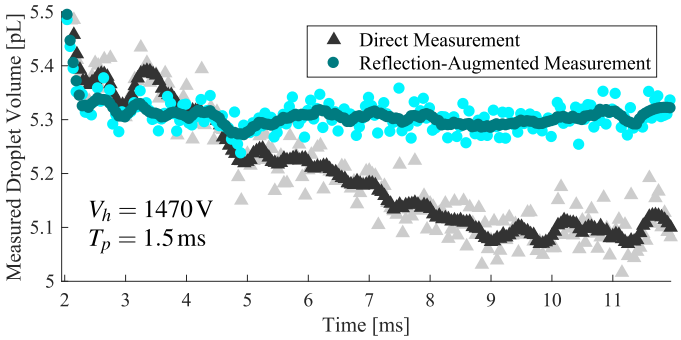

Figure 6. Retraction-stage droplet volume measurement taken by direct and reflection-augmented measurement techniques. Light and dark points represent raw and filtered data, respectively. As $\mathcal{V}_d$ is expected to be constant during retraction, this plot illustrates the reflection-augmented technique's superiority in that it maintains a roughly constant value of 5.3 pL after the transient (i.e. for $t \geq 2.5\,\mathrm{ms}$), while the direct measurement steadily decreases until about $t = 9\,\mathrm{ms}$.

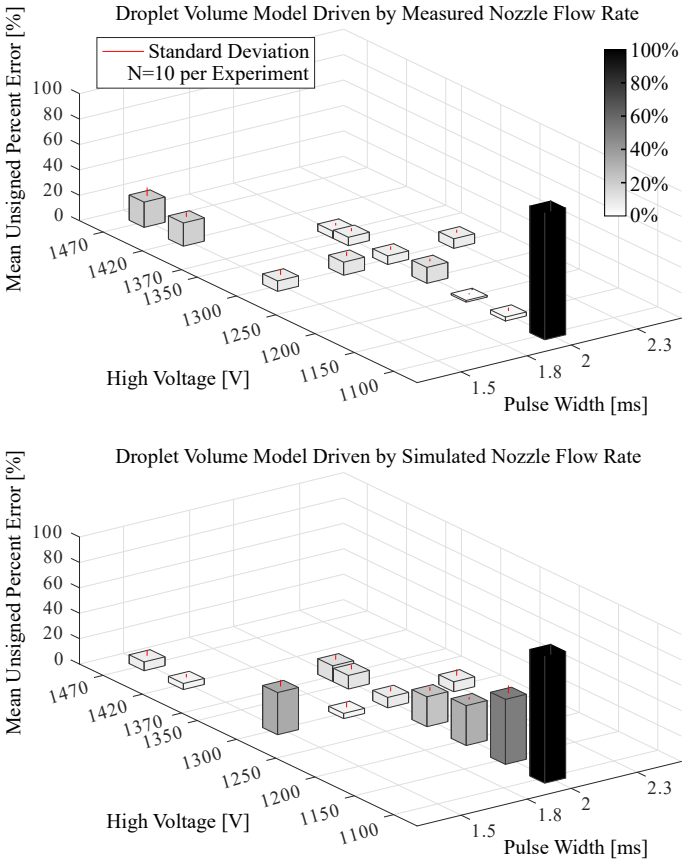

Figure 7. Percent error in final deposited droplet volume, $\mathcal{V}_d(t_r)$, using measured and simulated Q. The lowest voltage experiment exceeds 100% error in both cases. Each bar represents the mean value of $N = 10$ samples. Measured Q results illustrate the high quality of equation (6) for all but the lowest voltage case. Simulated Q results illustrate increased error associated with increased uncertainty in the cascaded model, motivating future flow rate modeling work.

5 RESULTS & DISCUSSION

5.1 Droplet Volume Measurement

Equations (11) and (12) show that the reflection-augmented image processing yields a 42% decrease in total variation of measured droplet volume time series data compared to direct measurement, with an associated standard deviation of 10%. This substantial performance improvement can be visualized through the example retraction-stage droplet volume time series in Figure 6, in which the direct measurement yields a steady decrease while the reflection-augmented measurement yields a relatively constant droplet volume.

However, in both measurement schemes there is a steep transient at the start of retraction. This arises from an inability of these measurement techniques to conserve volume over the collapse of the relatively tall and thin droplet tail (observable in Figure 5, right) into the larger and wider main droplet body.

Thus, these results demonstrate that the reflection-augmented volume measurement scheme is an effective tool that may be useful for future e-jet printing research, but does not address every artifact associated with video-based measurement, which may serve as the subject of future investigations.

5.2 Deposited Droplet Volume Error

Figure 7 presents the mean percent error in the final droplet volume as computed by equation (14), for each experiment. The experiment of lowest high voltage ($V_h = 1100\,\mathrm{V}$) clearly represents an outlier in this data, having a percent error of 130% for the predictions driven by measured nozzle flow rate and 170% for the predictions using simulated nozzle flow rate, more than triple the next highest percent error.

To better discuss this outlying experiment, time series plots of $\mathcal{V}_d(t)$ and a plot of each trial's estimated jet break position, h_b, versus V_h are presented in Figures 8 and 9, respectively. From the time series plot, one observes that the reset—the initial step change from zero to non-zero volume—is the most clearly erroneous feature of the low V_h time series. The reset causes a large overestimation of the initial volume in the contiguity stage that cannot be compensated for by the contiguity dynamics models, which only capture the change in droplet volume from the beginning to the end of contiguity.

The plot of h_b in Figure 9 lends insight into why this reset error may arise. While the experiments well within the subcritical jetting regime (those from 1150 V to 1420 V) show comparable h_b values, the experiment of lowest V_h shows a jet break position markedly closer to the substrate. Because h_b marks the upper boundary of the droplet control volume (a condition necessary for droplet flow rate to be zero after the jet breaks), this lowered jet break position substantially reduces the fraction of total vol-

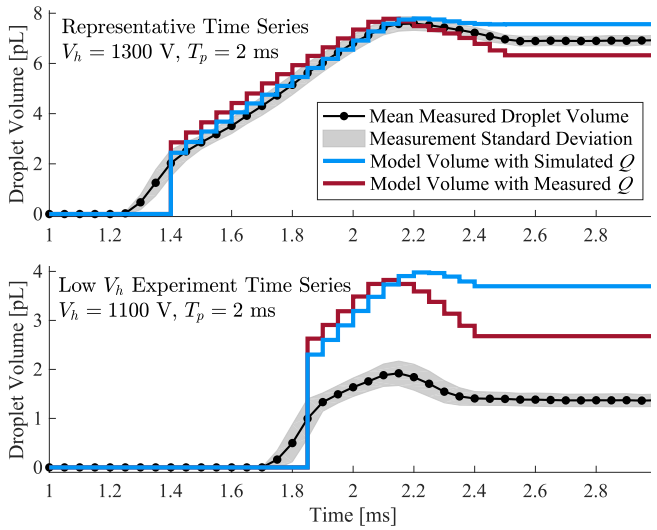

Figure 8. Time series plots of droplet volume $\mathcal{V}_d$ for a representative experiment and the experiment of lowest high voltage V_h. Plotted measured data is the mean of the validation data ($N = 10$ samples for each time series) with an envelope of plus or minus the standard deviation. The data suggests that the reset is the main source of error in low V_h experiments.

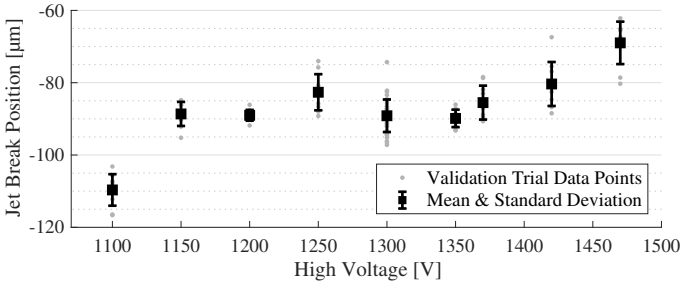

Figure 9. Jet break positions of each experiment's validation data against high voltage. The nozzle outlet is located at 0 µm and the substrate at −150 µm. $N = 10$ samples for all high voltages except $V_h = 1300$ V, for which $N = 40$ samples because four pulse widths are tested at $V_h = 1300$ V. The modest spread of data points at $V_h = 1300$ V suggests that high voltage (equivalent to the difference between high and low voltage in this data set) has a greater influence on jet break position than pulse width in the subcritical jetting regime.

ume that is in the droplet control volume at the first moment of contiguity. This change in the fraction of total volume is not accounted for by the reset model (5), which assumes only the total volume itself is changing (e.g. because of jet diameter variations over applied voltage).

Because the given model structure does not account for the changing jet break position near the boundaries of the subcritical jetting regime, the low V_h experiment is deemed to be outside the applicable domain of the model, and is thus removed from the aggregate model error data, given in Figure 10. The lower error

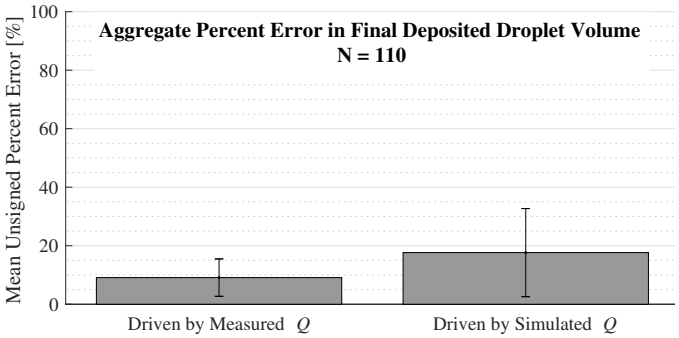

Figure 10. Mean unsigned percent error and standard deviation (given by error bars) of final droplet volume over all validation trials except those of lowest high voltage ($N = 110$ samples).

yielded when the droplet volume model is driven by measured nozzle flow rate illustrates the validity of the Q-to-$\mathcal{V}_d$ model (6). When equation (6) is driven by the nozzle flow rate simulated by equation (10), making a complete model from V to $\mathcal{V}_d$, the error increases. This is due to increased model uncertainty associated with equation (10) and its cascading with equation (6). While reducing this model uncertainty will be an important future endeavor, these results demonstrate the foundation of a dynamical V-to-$\mathcal{V}_d$ model that may be integrated with iterative learning control (such as in [20]) for the sake of e-jet printing control.

6 CONCLUSION

This paper presents a hybrid system model framework for dynamical droplet volume modeling in e-jet printing based on contiguity of the fluid jet between the nozzle and the substrate. This overarching modeling framework involves the contributions of several novel model elements whose structures are motivated by physical analysis of the material ejection process. These contributions include a new droplet control volume definition enabling the treatment of droplet volume as a dynamically evolving parameter, a dynamical mapping between nozzle flow rate and droplet volume during contiguity, and a reset map circumventing the need for dynamical modeling of droplet volume before contiguity, when data is of limited availability. Additionally, this paper contributes a new computer vision method for extracting time series volume data from videos that, while simple, substantially improves the consistency of volume measurements. These contributions are validated with physical experiments that show good model performance in the interior of the subcritical jetting regime, but reveal system behaviors not captured by the model towards the boundaries of the subcritical jetting regime, specifically unmodeled changes in the jet break position.

The presented work thus represents an important step towards model-based control of deposited droplet volume in e-jet printing. To further pursue this goal, future work will focus on

refining the reset model to account for the entire subcritical jetting regime, and on finding an ideal balance between simplicity and fidelity in applied-voltage-to-nozzle-flow-rate models.

REFERENCES

[1] Han, Y., Wei, C., and Dong, J., 2015. "Droplet formation and settlement of phase-change ink in high resolution electrohydrodynamic (EHD) 3D printing". *Journal of Manufacturing Processes,* ***20***(3), pp. 485–491.

[2] Carter, W., Popell, G. C., Samuel, J., and Mishra, S., 2014. "A Fundamental Study and Modeling of the Micro-Droplet Formation Process in Near-Field Electrohydrodynamic Jet Printing". *Journal of Micro and Nano-Manufacturing,* ***2***(2), p. 021005.

[3] Park, J.-U., Hardy, M., Kang, S. J., Barton, K., Adair, K., Mukhopadhyay, D. K., Lee, C. Y., Strano, M. S., Alleyne, A. G., Georgiadis, J. G., Ferreira, P. M., and Rogers, J. A., 2007. "High-resolution electrohydrodynamic jet printing". *Nature Materials,* ***6***(10), pp. 782–789.

[4] Spiegel, I., Kovalenko, I., Hoelzle, D., Sammons, P. M., and Barton, K. L., 2017. "Hybrid modeling and identification of jetting dynamics in electrohydrodynamic jet printing". In 2017 IEEE Conference on Control Technology and Applications (CCTA), pp. 695–701.

[5] Jang, Y., Hartarto Tambunan, I., Tak, H., Dat Nguyen, V., Kang, T., and Byun, D., 2013. "Non-contact printing of high aspect ratio Ag electrodes for polycrystalline silicone solar cell with electrohydrodynamic jet printing". *Applied Physics Letters,* ***102***(12), p. 123901.

[6] Wang, K., and Stark, J., 2010. "Direct fabrication of electrically functional microstructures by fully voltage-controlled electrohydrodynamic jet printing of silver nano-ink". *Applied Physics A,* ***99***(4), pp. 763–766.

[7] Lee, S., Kim, J., Choi, J., Park, H., Ha, J., Kim, Y., Rogers, J., and Paik, U., 2012. "Patterned oxide semiconductor by electrohydrodynamic jet printing for transparent thin film transistors". *Applied Physics Letters,* ***100***, pp. 102108:1–4.

[8] Choi, K., Zubair, M., and Dang, H., 2014. "Characterization of flexible temperature sensor fabricated through drop-on-demand electrohydrodynamics patterning". *Japanese Journal of Applied Physics,* ***53***, pp. 05HB02:1–5.

[9] Park, J.-U., Lee, J., Paik, U., Lu, Y., and Rogers, J., 2008. "Nanoscale patterns of oligonucleotides formed by electrohydrodynamic jet printing with applications in biosensing and nanomaterials assembly". *Nano Letters,* ***8***(12), pp. 4210–4216.

[10] Poellmann, M., Barton, K., Mishra, S., and Johnson, A. W., 2011. "Patterned hydrogel substrates for cell culture with electrohydrodynamic jet printing". *Macromolecular Bioscience,* ***11***, pp. 1164–1168.

[11] Sammons, P., Bollineni, S., Sibal, R., and Barton, K., 2017. "Temperature and Humidity Variation Effect on Process Behavior in Electrohydrodynamic Jet Printing of a Class of Optical Adhesives". In 28th Annual International Solid Freeform Fabrication Symposium, University of Texas, Austin, pp. 1784–1794.

[12] Afkhami, Z., Pannier, C. P., Aarnoudse, L., Hoelzle, D., and Barton, K., 2021. "Spatial Iterative Learning Control for Multi-material Three-Dimensional Structures". *ASME Letters in Dynamic Systems and Control,* ***1***(1), p. 011011.

[13] Wang, Z., Pannier, C. P., Barton, K., and Hoelzle, D. J., 2018. "Application of robust monotonically convergent spatial iterative learning control to microscale additive manufacturing". *Mechatronics,* ***56***, pp. 157–165.

[14] Altin, B., Wang, Z., Hoelzle, D. J., and Barton, K., 2019. "Robust Monotonically Convergent Spatial Iterative Learning Control: Interval Systems Analysis via Discrete Fourier Transform". *IEEE Transactions on Control Systems Technology,* ***27***(6), pp. 2470–2483.

[15] Wright, G. S., Krein, P. T., and Chato, J. C., 1993. "Factors affecting dynamic electrical manipulation of menisci". *IEEE Transactions on Industry Applications,* ***29***(1), pp. 103–112.

[16] Yang, J., Kim, H., Cho, B., and Chung, J., 2014. "Modeling of sessile droplet oscillation on electrohydrodynamic jetting nozzle at constant back pressure". *Journal of Mechanical Science and Technology,* ***28***(7), pp. 2815–2823.

[17] Spiegel, I. A., Sammons, P., and Barton, K., 2019. "Hybrid Modeling of Electrohydrodynamic Jet Printing". *IEEE Transactions on Control Systems Technology*.

[18] Heemels, W. P. M. H., De Schutter, B., and Bemporad, A., 2001. "Equivalence of hybrid dynamical models". *Automatica,* ***37***(7), pp. 1085–1091.

[19] Lee, A., Jin, H., Dang, H. W., Choi, K. H., and Ahn, K. H., 2013. "Optimization of experimental parameters to determine the jetting regimes in electrohydrodynamic printing". *Langmuir,* ***29***(44), pp. 13630–13639.

[20] Spiegel, I. A., and Barton, K., 2019. "A Closed-Form Representation of Piecewise Defined systems and their Integration with Iterative Learning Control". In 2019 IEEE Annual American Control Conference (ACC), IEEE, pp. 2327–2333.